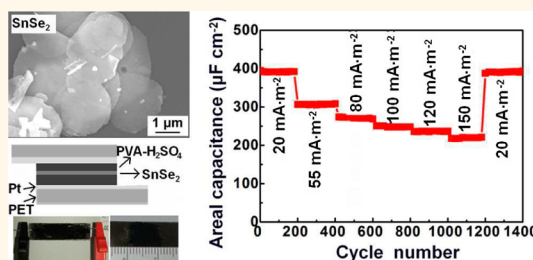


# Two-Dimensional Tin Selenide Nanostructures for Flexible All-Solid-State Supercapacitors

Chunli Zhang,<sup>†</sup> Huanhuan Yin,<sup>†</sup> Min Han,<sup>†,‡,\*</sup> Zhihui Dai,<sup>†</sup> Huan Pang,<sup>\*,†,‡,\*</sup> Yulin Zheng,<sup>†</sup> Ya-Qian Lan,<sup>†</sup> Jianchun Bao,<sup>†,\*</sup> and Jianmin Zhu<sup>‡</sup>

<sup>†</sup>Jiangsu Key Laboratory of Biofunctional Materials, School of Chemistry and Materials Science, Nanjing Normal University, Nanjing 210023, People's Republic of China, <sup>‡</sup>State Key Laboratory of Coordination Chemistry, Nanjing National Laboratory of Solid State Microstructures, Nanjing University, Nanjing 210093, People's Republic of China, and <sup>‡</sup>Key Laboratory for Clearer Energy and Functional Materials of Henan Province, College of Chemistry and Chemical Engineering, Anyang Normal University, Anyang 455001, People's Republic of China

**ABSTRACT** Due to their unique electronic and optoelectronic properties, tin selenide nanostructures show great promise for applications in energy storage and photovoltaic devices. Despite the great progress that has been achieved, the phase-controlled synthesis of two-dimensional (2D) tin selenide nanostructures remains a challenge, and their use in supercapacitors has not been explored. In this paper, 2D tin selenide nanostructures, including pure SnSe<sub>2</sub> nanodisks (NDs), mixed-phase SnSe–SnSe<sub>2</sub> NDs, and pure SnSe nanosheets (NSs), have been synthesized by reacting SnCl<sub>2</sub> and trioctylphosphine (TOP)-Se with borane-*tert*-butylamine complex (BTBC) and 1,3-dimethyl-3,4,5,6-tetrahydro-2(1*H*)-pyrimidinone. Utilizing the interplay of TOP and BTBC and changing only the amount of BTBC, the phase-controlled synthesis of 2D tin selenide nanostructures is realized for the first time. Phase-dependent pseudocapacitive behavior is observed for the resulting 2D nanostructures. The specific capacitances of pure SnSe<sub>2</sub> NDs (168 F g<sup>−1</sup>) and SnSe NSs (228 F g<sup>−1</sup>) are much higher than those of other reported materials (*e.g.*, graphene-Mn<sub>3</sub>O<sub>4</sub> nanorods and TiN mesoporous spheres); thus, these tin selenide materials were used to fabricate flexible, all-solid-state supercapacitors. Devices fabricated with these two tin selenide materials exhibited high areal capacitances, good cycling stabilities, excellent flexibilities, and desirable mechanical stabilities, which were comparable to or better than those reported recently for other solid-state devices based on graphene and 3D GeSe<sub>2</sub> nanostructures. Additionally, the rate capability of the SnSe<sub>2</sub> NDs device was much better than that of the SnSe NS device, indicating that SnSe<sub>2</sub> NDs are promising active materials for use in high-performance, flexible, all-solid-state supercapacitors.



**KEYWORDS:** tin selenide · 2D nanostructures · phase control · electrochemistry · supercapacitors · flexibility

The fabrication of high-efficiency energy storage devices has attracted widespread attention due to ever-increasing demands for renewable energy.<sup>1</sup> Supercapacitors (SCs), also known as electrochemical capacitors, are promising energy storage devices because they offer higher power densities, longer operating lifespans, and better safety tolerances than batteries.<sup>2–7</sup> Recently, substantial efforts have focused on flexible and thin SCs to meet growing requirements for lightweight portable electronic devices, including devices capable of being rolled up.<sup>8–14</sup> For these applications, it is necessary to find appropriate electroactive materials and integrate them into specific device configurations. Active materials with hierarchical

pores, and tubular or layered structures, can promote charge transport and ion diffusion, enhancing power density and cycling stability of SCs.<sup>15</sup> Additionally, the composition and phase of certain pseudocapacitive materials affect energy storage in devices fabricated from these materials.<sup>16</sup> Certain nanostructured materials, such as carbon nanotubes,<sup>17</sup> graphene and its composites,<sup>18–24</sup> layered hydroxides and oxides,<sup>25–29</sup> and metal/oxide hybrids,<sup>30</sup> have been developed for use in SCs with desirable properties. The members of one class of important functional nanomaterials, two-dimensional (2D) layered metal chalcogenides (LMCs), exhibit unique electronic structures and physical properties due to their special geometric structures with weak

\* Address correspondence to 07203@njnu.edu.cn (M. Han); baojianchun@njnu.edu.cn (J. C. Bao); huanpangchem@hotmail.com (H. Pang).

Received for review January 22, 2014 and accepted March 6, 2014.

Published online March 06, 2014  
10.1021/nn5004315

© 2014 American Chemical Society

interlayer Van de Waals coupling, variable composition, and rich phase structure<sup>31–35</sup> and thus provide a large library of materials for potential applications in flexible energy storage devices. However, only VS<sub>2</sub> nanosheets (NSs) have been used as active materials in high-performance flexible SCs with in-plane configuration.<sup>36</sup>

Tin selenides, which belong to one class of typical LMCs and are narrow band gap semiconductors, are promising candidates for use in infrared optoelectronic devices,<sup>37</sup> solar cells,<sup>38,39</sup> memory switching devices,<sup>40</sup> and anodes for lithium-ion batteries.<sup>41</sup> However, problems with the composition or phase of these materials are encountered frequently during their synthesis.<sup>41,42</sup> The two main phases of tin selenide materials are hexagonal-phase SnSe<sub>2</sub> and orthorhombic-phase SnSe. By selecting special organic Sn or Se precursors and carefully monitoring the reaction conditions, specific SnSe<sub>2</sub> and SnSe nanostructures have been synthesized,<sup>38–44</sup> but very few 2D tin selenide nanostructures have been prepared. To the best of our knowledge, only hexagonal SnSe<sub>2</sub> nanodisks (NDs),<sup>41,45</sup> square SnSe NSs,<sup>46</sup> and single-layer SnSe NSs<sup>47</sup> have been synthesized. Despite these successes, the phase-controlled synthesis of 2D tin selenide nanostructures remains a challenge, and no studies of these nanostructures in SCs have been reported. On the basis of the excellent electronic properties of 2D layered crystal structures and their unique mechanical flexibility,<sup>48,49</sup> synthesizing 2D tin selenide nanostructures and exploring their applications in SCs are of great importance.

In this paper, we report results for the phase-controlled synthesis of 2D tin selenide nanostructures and their use in flexible, all-solid-state SCs. The synthesis is based on a simple one-pot chemical route, *i.e.*, heating common SnCl<sub>2</sub> and trioctyl-phosphine (TOP)-Se precursors in the presence of borane-*tert*-butylamine complex (BTBC) and 1,3-dimethyl-3,4,5,6-tetrahydro-2(1*H*)-pyrimidinone (DMPU). The significant features of our synthesis are as follows: (1) DMPU is an environmentally friendly solvent and a weak oxidant that triggers an increase in the valence of tin from +2 to +4; (2) BTBC is a reducing agent that binds with TOP to form unique surface ligands that permit lateral growth while passivating vertical growth along the *c*-axis of SnSe<sub>2</sub>; (3) by simply adjusting the amount of BTBC, it is possible to selectively obtain pure SnSe<sub>2</sub> NDs, SnSe NSs, and mixed-phase SnSe–SnSe<sub>2</sub> NDs. Phase-dependent pseudocapacitive behaviors are observed for these 2D nanostructures. Due to their high specific capacitances, pure SnSe<sub>2</sub> NDs (168 F g<sup>–1</sup>) and SnSe NSs (228 F g<sup>–1</sup>) are chosen as active materials to fabricate flexible, all-solid-state SCs. The areal capacitances, cycling stabilities, rate capabilities, mechanical flexibilities, and stabilities of these fabricated solid-state devices are studied systematically. In this study, the

overall performance of the SnSe<sub>2</sub> NDs device is superior to that of a device based on SnSe NSs, as well as other results for devices based on graphene<sup>9</sup> and 3D GeSe<sub>2</sub> nanostructures,<sup>50</sup> indicating that SnSe<sub>2</sub> NDs are promising candidate materials for use in high-performance, flexible, all-solid-state SCs.

## RESULTS AND DISCUSSION

Figure 1A shows the X-ray energy dispersive spectra (EDS) patterns of as-synthesized SnSe<sub>2</sub> NDs and SnSe NSs. Except for small C and O peaks that originate from adsorbed organic capping reagents or air, only Sn and Se are detected. By integration calculation, the atomic ratios of Sn to Se are approximately 1:2 and 1:1 in the two samples, indicating that they are likely to be SnSe<sub>2</sub> and SnSe, respectively. Further evidence comes from X-ray diffraction (XRD) analysis, shown in Figure 1B. Compared with Joint Committee on Powder Diffraction Standard Cards (JCPDS-89-2939 and JCPDS-72-1460), the two samples can be assigned to hexagonal-phase SnSe<sub>2</sub> and orthorhombic-phase SnSe. The corresponding XPS fine spectra for Sn 3d and Se 3d (Supporting Information, Figure S1) confirm that the valences of Sn in the two samples are +4 and +2, and the valence of Se is –2 in both cases.<sup>39,41,42</sup> The morphologies and microstructures of those two samples are examined by field-emission scanning electron microscopy (FE-SEM), atomic force microscopy (AFM), and transmission electron microscopy (TEM), respectively. Figure 1C and D show the low- and high-magnification FE-SEM images of the SnSe<sub>2</sub> NDs, respectively. In Figure 1C, many 2D pancake-like nanostructures can be observed. The lateral width or diameter of those NDs is approximately 2–3 μm, and their average thickness, measured from Figure 1D, is about 8 nm. Further atomic force microscopy (AFM) characterization (Figure S2A,B) identifies that the exact thickness of the SnSe<sub>2</sub> NDs is 9 nm. The corresponding TEM image is given in Figure 1E. The selected area electron diffraction (SAED) pattern of the SnSe<sub>2</sub> NDs shows well-defined spots, indicating that they are single crystals. The related HRTEM analysis (Figure 1F) for an individual ND exhibits clear lattice fringes, and the lattice spacing is approximately 1.94 Å, corresponding to the interplanar separation of (110) facets of hexagonal-phase SnSe<sub>2</sub>. As for the SnSe sample, sheet-like nanostructures with some wrinkles are observed (Figure 1G), and their thickness is estimated to be about 3 nm from their turnup edges. Further AFM measurement (Figure S2C,D) reveals that the actual thickness of the SnSe NSs is 2 nm. The corresponding HRTEM analysis (Figure 1H) shows clear lattice fringes, and the lattice spacing is approximately 3.05 Å, assigned to the interplanar separation of the (110) facets of orthorhombic-phase SnSe. As evidenced by SAED analysis, these SnSe NSs are also single crystals. In addition, Fourier transform infrared (FT-IR) spectra tests (Figure S3)

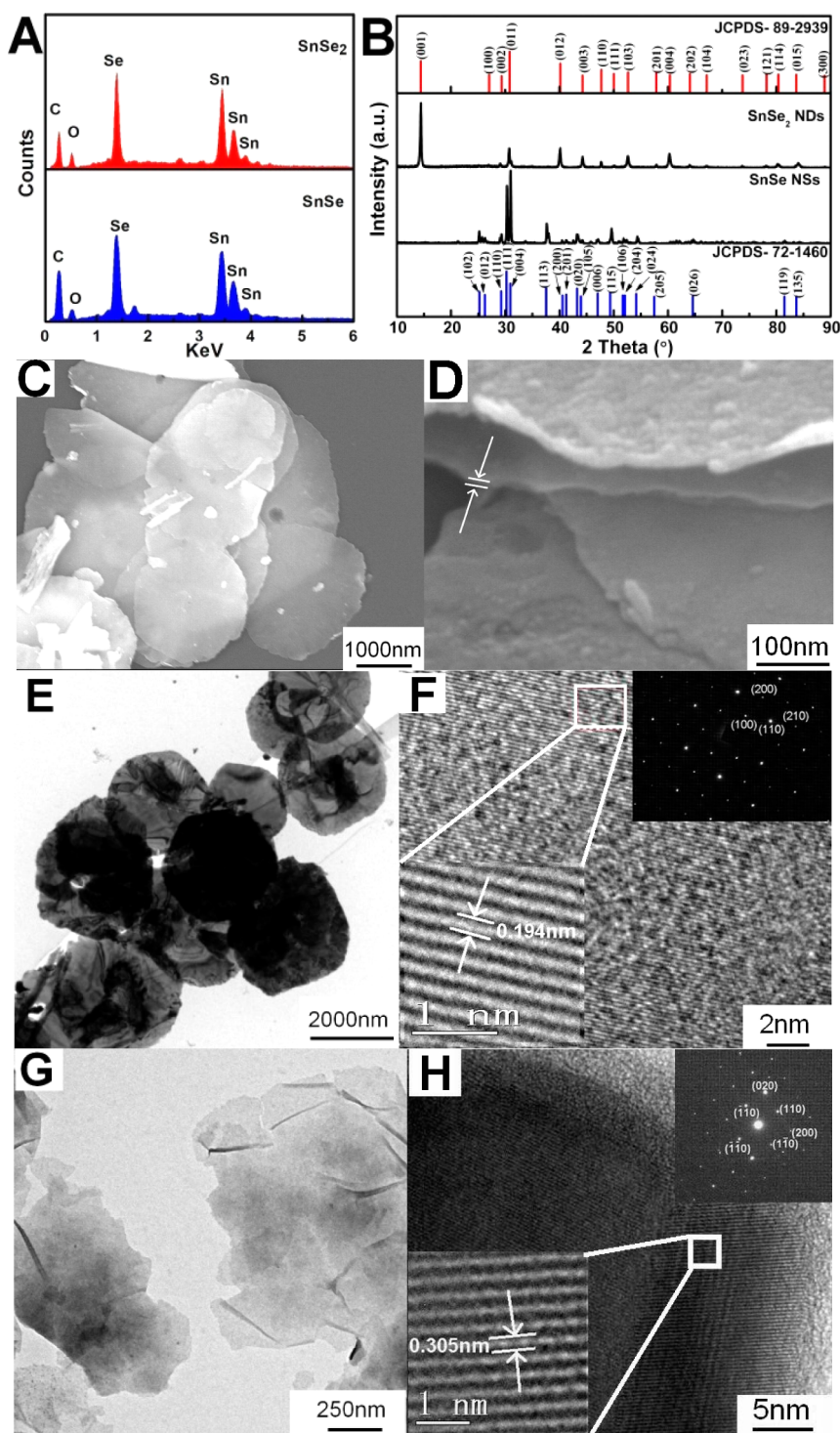


**Figure 1.** (A) EDS and (B) XRD patterns of  $\text{SnSe}_2$  NDs (top) and  $\text{SnSe}$  NSs (bottom). (C) Low- and (D) high-magnification FE-SEM images of  $\text{SnSe}_2$  NDs. (E) TEM and (F) HRTEM images of  $\text{SnSe}_2$  NDs. The SAED pattern and magnified lattice fringes are shown in the upper right and lower left corners of (F), respectively. (G) TEM and (H) HRTEM images of  $\text{SnSe}$  NSs. The SAED pattern and magnified lattice fringes are shown in the upper right and lower left corners of (G), respectively.

demonstrate that both the  $\text{SnSe}_2$  NDs and  $\text{SnSe}$  NSs are covered with a layer of surface ligand (the combination of TOP and BTBC).

To gain insight into the formation mechanism of these 2D tin selenide nanostructures, a series of control experiments were performed. The valence of tin in our

raw material is +2, which does not explain why  $\text{SnSe}_2$  is obtained in our synthesis. Is tin oxidized by  $\text{O}_2$  present in air? To investigate this question, a control experiment was performed by introducing high-purity Ar gas to purge air from the reaction vessel, after which the same  $\text{SnSe}_2$  ND synthesis procedure was followed.

Under this circumstance, the product is still SnSe<sub>2</sub> NDs. Thus, the influence of O<sub>2</sub> in air can be excluded. Considering that the solvent (DMPU) contains a ketone group and has some oxidative capacity, while SnCl<sub>2</sub> is a strong reducing agent, we attribute the increase in the valence of tin to the redox reaction between SnCl<sub>2</sub> and DMPU. Further evidence comes from another control experiment in which 1-ocadecene (no oxidative ability) was used in place of DMPU and the other conditions were kept unchanged. Only quasi-1D ribbon-like SnSe nanocrystals were generated in this case (Figure S4), confirming the above deduction. These results reveal that DMPU is not only a solvent but also a weak oxidizing agent in the synthesis of SnSe<sub>2</sub> NDs. Additionally, the TOP and BTBC also have significant impacts on the microstructure and phase of the final product. For example, without TOP and using only BTBC (100 mg) as the capping reagent, large and thick SnSe<sub>2</sub> disks with a diameter of 8–9 μm were formed (Figure S5A,B), while without BTBC and using only TOP (0.5 mL) as the capping reagent, the product was identified to be small-sized SnSe nanoparticle assemblies (Figure S5 C–D). Keeping the original amount of TOP and increasing BTBC from 100 to 200 mg yielded a mixed-phase, SnSe–SnSe<sub>2</sub> hexagonal ND (Figure S6). Further increasing BTBC to 500 mg generated pure SnSe NSs. The phenomena that led to the formation of these different products may have resulted from the use of TOP and BTBC. In combination, TOP and BTBC can form donor–acceptor-type complexes due to rich electrons on P and deficient electrons on B. Excess TOP leads to the extraction of Se<sup>2–</sup> from SnSe<sub>2</sub> to generate SnSe.<sup>51</sup> BTBC is not only a capping reagent that promotes the formation of disk-like structures but also a reducing agent that reduces Se powder to Se<sup>2–</sup> ions and partly or completely reduces SnSe<sub>2</sub> to SnSe. On the basis of these results along with SAED and HRTEM analysis (Figure 1F), we conclude that the combination of TOP and BTBC can efficiently passivate growth along the *c*-axis of SnSe<sub>2</sub> and facilitate the formation of 2D NDs. By combining TOP and BTBC and simply changing the amount of BTBC, the phase-controlled synthesis of 2D tin selenide nanostructures can be performed easily using the synthetic protocol described in this paper.

The electrochemical properties of the produced 2D tin selenide nanostructures were first evaluated in a three-electrode system using a 6 M KOH solution as the electrolyte. Figure 2A,B shows representative cyclic voltammetry (CV) plots for SnSe<sub>2</sub> NDs and SnSe NSs recorded at scan rates ranging from 5 to 100 mV s<sup>–1</sup>. One pair of redox peaks corresponding to the reversible reaction of Sn<sup>2+</sup> ↔ Sn<sup>4+</sup> can be observed clearly within 0–0.45 V (vs SCE) for SnSe<sub>2</sub> NDs and 0–0.6 V (vs SCE) for SnSe NSs, showing obvious pseudocapacitive features. At higher scan rates, the peak currents of both SnSe<sub>2</sub> NDs and SnSe NSs increased, suggesting that these materials are beneficial to fast redox reactions.

To further evaluate the potential applications of SnSe<sub>2</sub> NDs and SnSe NSs as electrodes for electrochemical SCs, galvanostatic charge–discharge measurements were carried out at various current densities from 0.5 to 10 A g<sup>–1</sup>, as shown in Figure 2C,D. The specific capacitances of the SnSe<sub>2</sub> ND electrodes (Figure 2E) calculated from the discharge branches are 168, 144, 120, 104, 86, and 80 F g<sup>–1</sup> at current densities of 0.5, 1, 2, 3, 5, and 10 A g<sup>–1</sup>, respectively, which are higher than those for graphene–Mn<sub>3</sub>O<sub>4</sub> nanorods,<sup>7</sup> activated nanoporous graphene,<sup>18</sup> and TiN mesoporous spheres<sup>52</sup> and similar to the results for CoS<sub>2</sub> nanoparticle electrodes.<sup>53</sup> For SnSe NSs electrodes, their specific capacitances (Figure 2F) of 228, 210, 179, 160, 135, and 117 F g<sup>–1</sup> at current densities of 0.5, 1, 2, 3, 5, and 10 A g<sup>–1</sup>, respectively, are higher than those for crumpled N-doped porous graphene NSs,<sup>21</sup> graphene–CoS<sub>2</sub> or MnO<sub>2</sub> nanocomposites,<sup>53,54</sup> and hollow CoS hexagonal NS electrodes.<sup>55</sup> With the increase of current density from 0.5 to 10 A g<sup>–1</sup>, the specific capacitances of the SnSe<sub>2</sub> NDs and SnSe NSs decrease only slightly, indicating that both materials possess good rate capability. At the same current density, their specific capacitances are distinct, indicating that the phase greatly affects their electrochemical energy storage capacity. Further evidence comes from the control experiment that used mixed-phase SnSe–SnSe<sub>2</sub> NDs as an active material. The corresponding CV and charge–discharge curves are provided in Figure S7. The specific capacitance of the mixed-phase product (31 F g<sup>–1</sup> at 0.5 A g<sup>–1</sup>) is much lower than that of the pure phase ones. The diverse performance of those 2D nanostructures may be attributed to their different microstructures and phase compositions, as well as their surface areas, which may provide distinct electroactive sites for redox reactions. On the basis of this determination, pure SnSe<sub>2</sub> NDs and pure SnSe NSs were chosen as active materials for further electrochemical tests and fabrication in desired solid-state devices.

The long-term cycling stability of SnSe<sub>2</sub> ND and SnSe NS electrodes was tested through cyclic charge–discharge processes at a current density of 1 A g<sup>–1</sup>. Figure 3A shows the first five charge–discharge cycles for SnSe<sub>2</sub> NDs. This device maintains 99.0% of its initial capacitance after 1000 charge–discharge cycles (the last five cycles are shown in Figure S8A), revealing good long-term cycling stability (Figure 3B). As for SnSe NS device, its first five charge–discharge cycles are given in Figure 3C. After 1000 cycles (the last five cycles are provided in Figure S8B), it retains 99.2% of its initial capacitance (Figure 3D), demonstrating good cycling performance. Under TEM examination, the SnSe<sub>2</sub> NDs and SnSe NSs exhibited only slight variation in their structures after cycling tests (Figure S9), which may be the origin of their good cyclic stability.

With the dream to develop flexible power sources, the stacked symmetric all-solid-state SCs were further



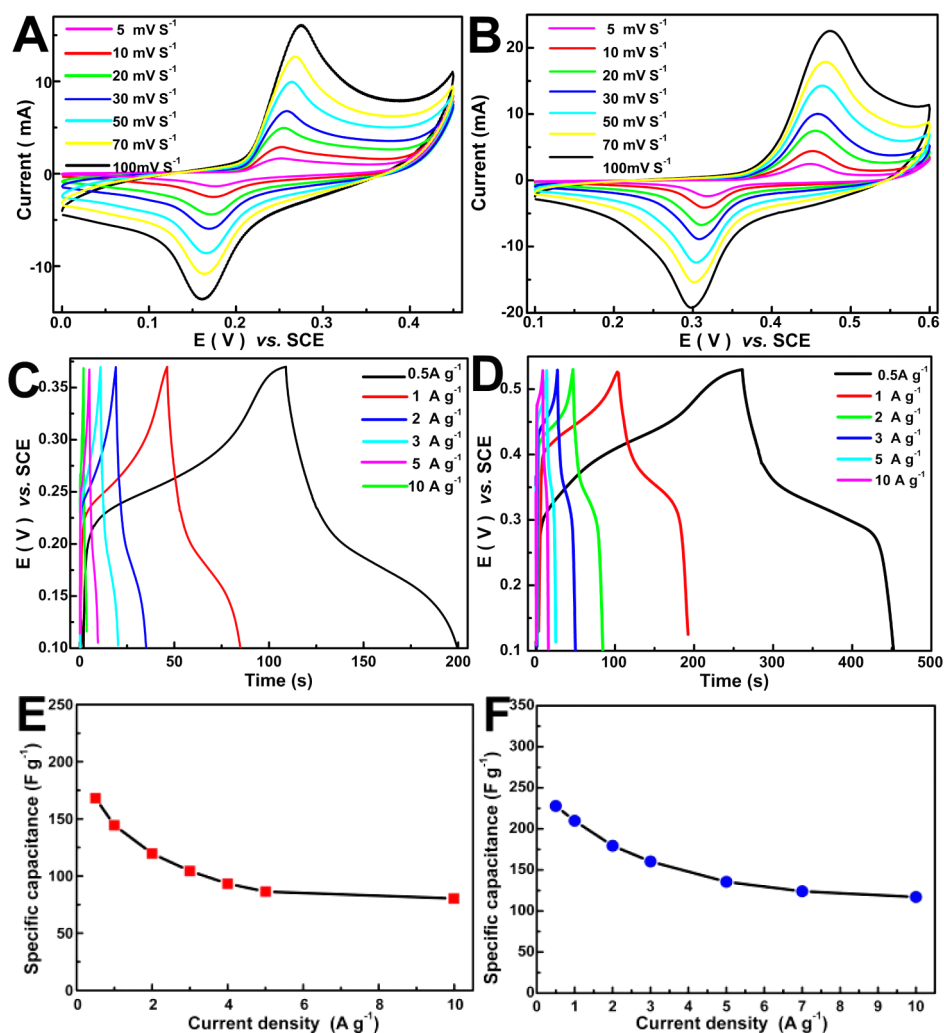


**Figure 2.** (A, B) CV results measured at different scan rates for (A) SnSe<sub>2</sub> NDs and (B) SnSe NSs. (C, D) Galvanostatic charge–discharge curves for (C) SnSe<sub>2</sub> NDs and (D) SnSe NSs. (E, F) Specific capacitances for (E) SnSe<sub>2</sub> NDs and (F) SnSe NSs at various current densities.

fabricated using SnSe<sub>2</sub> NDs and SnSe NSs as active materials, which were identified as SnSe<sub>2</sub> NDs-SSCs and SnSe NSs-SSCs. The polymer gel (polyvinyl alcohol-H<sub>2</sub>SO<sub>4</sub>) served as both the separator and the solid electrolyte. The detailed configurations of those two solid-state devices are shown in Figure 4A,B. For both devices, the working area was 1.0 cm<sup>2</sup>. The CV plots of SnSe<sub>2</sub> NDs-SSCs in the potential range from −0.4 to 0.4 V (Figure 4C) are symmetric and almost rectangular because of the surface electrosorption of H<sup>+</sup> and the consecutive reversible surface redox reactions of SnSe<sub>2</sub> NDs by means of H<sup>+</sup> intercalation/detercalation. The absence of redox peaks implies that the SSCs charged and discharged at a pseudoconstant rate during the voltammetric cycles.<sup>56,57</sup> Similar CV features are observed in the potential window from −0.6 to 0.6 V for SnSe NSs-SSCs, where the peak shapes are even closer to rectangular (Figure 4D).

Moreover, the galvanostatic charge–discharge measurements of those solid-state devices were performed at current densities ranging from 20 to

150 mA m<sup>−2</sup> (Figure S10A,B). Their specific capacitance (normalized by area) *versus* current density curves are given in Figure 4E,F. For SnSe<sub>2</sub> NDs-SSCs, the areal capacitance at 100 mA m<sup>−2</sup> is calculated to be 250 μF cm<sup>−2</sup>, which is 62% of its initial capacitance (406 μF cm<sup>−2</sup>) at 20 mA m<sup>−2</sup>. This decrease in capacitance may be attributed to the discrepancy that results from the insertion/deinsertion behavior of ions from the electrolyte to the electrodes.<sup>58</sup> The results for SnSe<sub>2</sub> NDs-SSCs show excellent electrochemical stability, and no capacitance loss is observed after 1000 cycles at constant current densities (Figure S10C). For SnSe NSs-SSCs, its areal capacitance at 100 mA m<sup>−2</sup> is 442 μF cm<sup>−2</sup>, which is much higher than that of SnSe<sub>2</sub> NDs-SSCs, graphene-based SSCs (394 μF cm<sup>−2</sup>),<sup>9</sup> and 3D GeSe<sub>2</sub> nanostructured SSCs (200 μF cm<sup>−2</sup>).<sup>50</sup> At constant current densities, almost no capacitive decrease occurs, even for 1000 charge–discharge cycles (Figure S10 D), indicating good electrochemical stability and capacitance retention ability under static conditions. However, compared with its initial capacitance

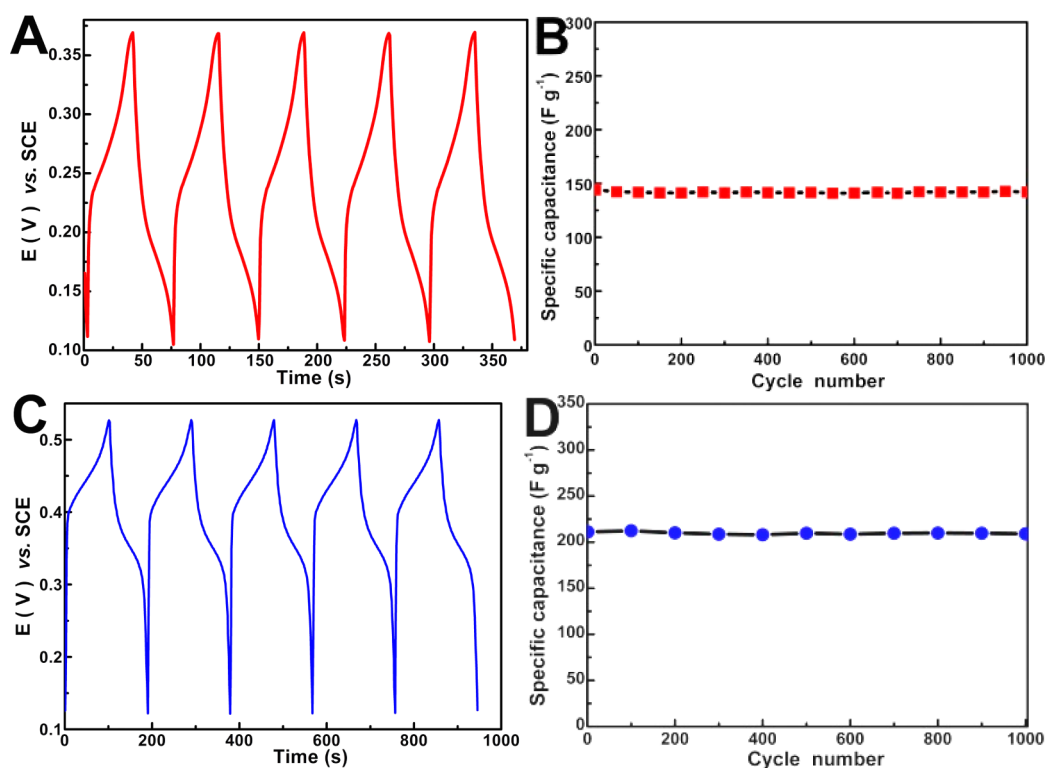


**Figure 3.** (A) Galvanostatic cycling behavior during the first 5 cycles and (B) evaluation of specific capacitance *versus* the number of cycles for a SnSe<sub>2</sub> ND electrode. (C) Galvanostatic cycling behavior during the first 5 cycles and (D) evaluation of specific capacitance *versus* the number of cycles for a SnSe NSs electrode.

(1176  $\mu\text{F cm}^{-2}$ ) at  $45 \text{ mA m}^{-2}$ , only 38% of the capacitance is reserved at the current density of  $100 \text{ mA m}^{-2}$ , implying that the rate capability of SnSe NSs-SSCs is weaker than that of SnSe<sub>2</sub> NDs-SSCs. Further evidence comes from cycling and rate capability tests with progressively varying current densities.

Figure 5 shows the areal capacitance *versus* cycle number curves for the two solid-state devices under gradually increasing current densities. After 200 continuous cycles at various current densities followed by a return to the initial current density, the initial capacitances of both solid-state devices could be recovered and maintained for another 200 cycles without a noticeable decrease. These data demonstrate that the constructed solid-state SCs can meet the requirements of long cycle life and good rate capability, which are important criteria for practical energy storage devices. The performance of SnSe<sub>2</sub> NDs-SSCs (Figure 5A) is comparable to or better than that of 3D GeSe<sub>2</sub> nanostructured SSCs.<sup>50</sup> For SnSe NSs-SSCs (Figure 5B), the capacitances decrease more rapidly with progressively increasing current densities from 45 to  $100 \text{ mA m}^{-2}$  than in the cases of SnSe<sub>2</sub> NDs-SSCs and 3D GeSe<sub>2</sub> nanostructured SSCs.<sup>50</sup> That is to say, the rate capability of SnSe NSs-SSCs is less than that of the other materials. On the basis of this result, the overall performance of SnSe<sub>2</sub> NDs-SSCs is better than that of SnSe NSs-SSCs.

Furthermore, to verify the flexibility and mechanical stability of the fabricated solid-state devices, they are

folded or bent at various angles, and their electrochemical responses are recorded accordingly. Figure 6 shows the CV response signals of SnSe<sub>2</sub> NDs-SSCs at different bending angles. Compared with the CV signal recorded at a scan rate of  $200 \text{ mV s}^{-1}$  without bending (Figure 6A), the CV curve is nearly unchanged when bent to  $60^\circ$  (Figure 6B). At greater bending curvatures of  $90^\circ$  (Figure 6C) and  $120^\circ$  (Figure 6D), there are no changes, and the CV plots are identical. Similar electrochemical response features were observed for SnSe NSs-SSCs at different bending angles, as illustrated in Figure S11. These results demonstrate that both of the fabricated devices possess excellent flexibility and mechanical stability.

## CONCLUSIONS

In summary, a facile method to synthesize 2D pure SnSe<sub>2</sub> NDs, SnSe NSs, and mixed-phase SnSe–SnSe<sub>2</sub> NDs has been developed by combining BTBC and TOP with DMPU as a solvent and weak oxidant. Taking advantage of the interaction between TOP and BTBC and simply adjusting the amount of BTBC, a phase-controlled synthesis of 2D tin selenide nanostructures has been performed easily for the first time. Phase-dependent pseudocapacitive behaviors are observed in those 2D tin selenide nanostructures. Among them, the specific capacitances (normalized by mass) of pure SnSe<sub>2</sub> NDs ( $168 \text{ F g}^{-1}$ ) and SnSe NSs ( $228 \text{ F g}^{-1}$ ) are much higher than that of the mixed-phase product

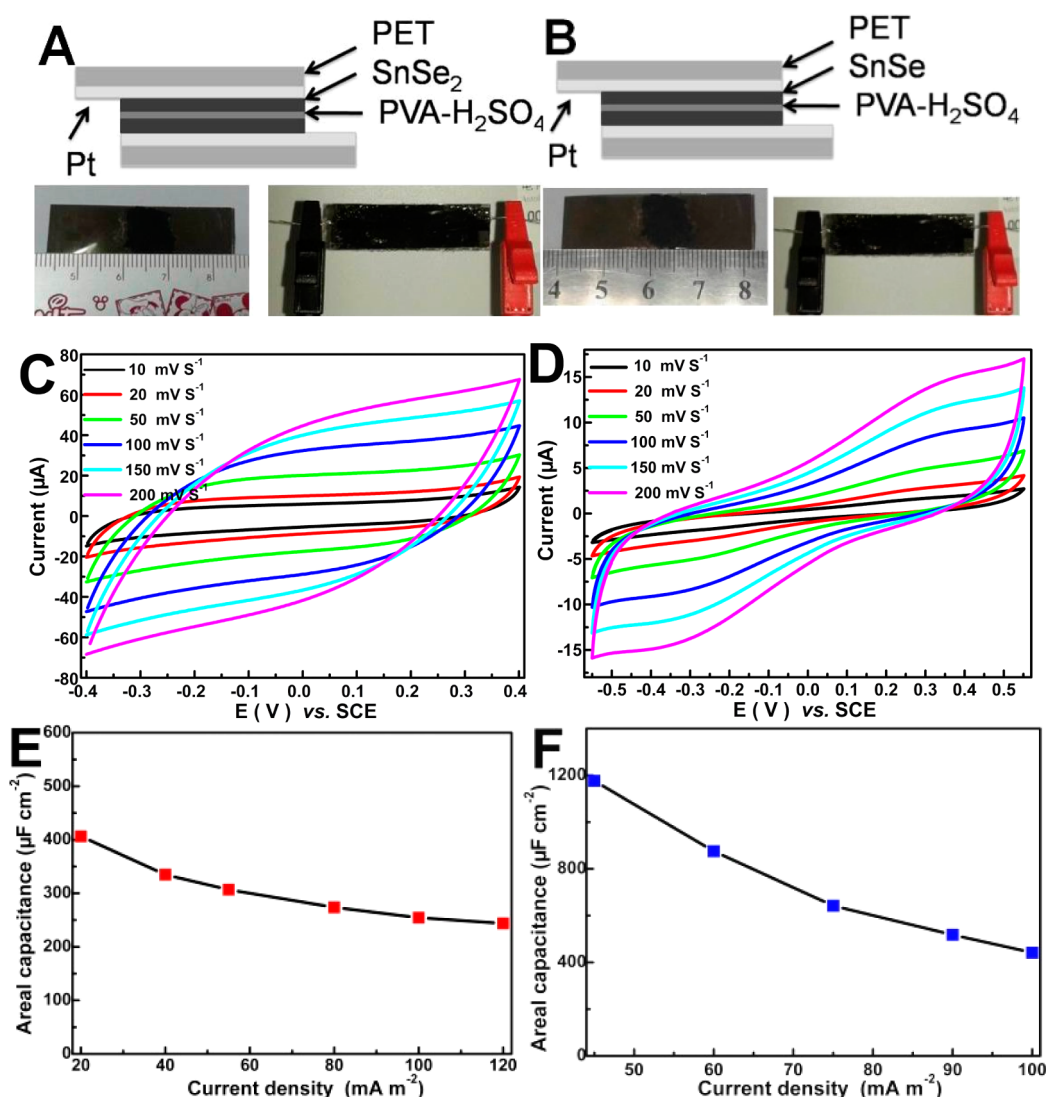


Figure 4. (A, B) Schematic diagrams (top) and photographs (bottom) of the stacked (A) SnSe<sub>2</sub> ND-SSC and (B) SnSe NSs-SSC devices. (C, D) CV curves of devices based on (C) SnSe<sub>2</sub> NDs-SSCs and (D) SnSe NSs-SSCs, measured at different scan rates. (E, F) Specific capacitances of devices based on (E) SnSe<sub>2</sub> NDs-SSCs and (F) SnSe NSs-SSCs at various current densities.

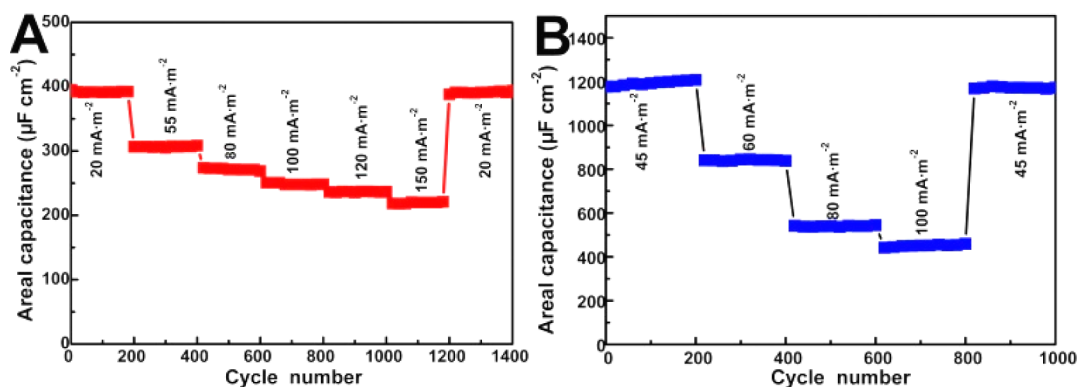
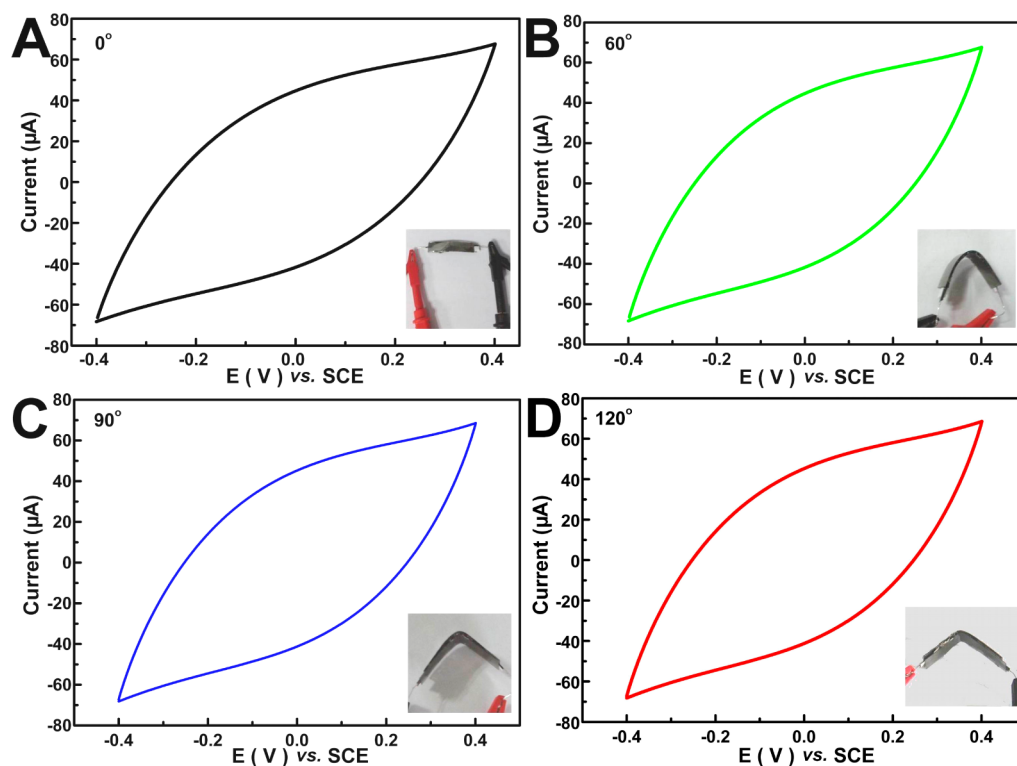


Figure 5. Cycling performance of (A) SnSe<sub>2</sub> ND-SSC and (B) SnSe NSs-SSC devices, measured by progressively varying the current density.

(31 F g<sup>-1</sup>) and other electrode materials (graphene-Mn<sub>3</sub>O<sub>4</sub> or CoS<sub>2</sub> nanocomposites, activated nanoporous graphene, TiN mesoporous spheres, crumpled

N-doped graphene, etc.). Thus, by using them as active materials, two stacked all-solid-state flexible devices, SnSe<sub>2</sub> NDs-SSCs and SnSe NSs-SSCs, are fabricated by



**Figure 6.** Flexibility and stability of a SnSe<sub>2</sub> ND-SSC device upon flexing evaluated by measuring CV curves at different bending angles: (A) 0°, (B) 60°, (C) 90°, and (D) 120°.

using PVA-H<sub>2</sub>SO<sub>4</sub> gel as the separator and solid electrolyte. The SnSe<sub>2</sub> NDs-SSCs exhibit better performance compared with that of SnSe NSs-SSCs as well as recently reported graphene and 3D GeSe<sub>2</sub> nanostructured devices, showing promise as a flexible power supply for driving small nanoelectronic devices in integrated nanosystems. Although the areal capacitance of our SnSe<sub>2</sub> ND-SSC device needs to be improved

relative to previously reported VS<sub>2</sub> NS in-plane SCs, it confirms that SnSe<sub>2</sub> NDs are another promising candidate in the LMC family for use in high-performance flexible SCs. Hybridizing them with other materials and optimizing their spatial arrangement as well as device configuration may greatly improve the capacitance or energy density of SnSe<sub>2</sub> ND based electrode materials. Further work on this is under way.

## METHODS

**Reagents and Materials.** Anhydrous SnCl<sub>2</sub> (>99%) and Se powder (>99.8%) were obtained from Sinopharm Chemical Reagent Co. Ltd. (Shanghai). The borane-*tert*-butylamine complex (97%), 1,3-dimethyl-3,4,5,6-tetrahydro-2(1*H*)-pyrimidinone (98%), tri-n-octylphosphine (>90%), and 1-octadecene (>90%) were purchased from Aldrich. The acetylene black (ATB), polytetrafluoroethylene (PTFE) dispersion (60%), polyvinyl alcohol (PVA), and poly(ethylene terephthalate) (PET) pieces were purchased from Alfa Aesar.

**Synthesis of SnSe<sub>2</sub> NDs.** In a typical synthesis, 40 mg of anhydrous SnCl<sub>2</sub>, 100 mg of BTBC, and 10 mL of DMPU were added to a clean 250 mL flask at room temperature. Then, 0.5 mL of TOP-Se stock solution, obtained by dissolving 0.316 g of Se powder in 10 mL of TOP, was added immediately to the flask. Next, the flask was placed in a reactor and heated to 240 °C at a rate of 5 °C min<sup>-1</sup> and maintained at that temperature for 30 min. Finally, the reactor was allowed to cool to room temperature. The raw product was separated by centrifugation and washed with heptane and absolute alcohol 3 or 4 times to remove byproducts. The product was dried under vacuum at 40 °C for 4 h and used for characterization and analysis.

**Synthesis of SnSe–SnSe<sub>2</sub> NDs and SnSe NSs.** The synthetic procedures for SnSe–SnSe<sub>2</sub> NDs and SnSe NSs were similar to the

above procedure for SnSe<sub>2</sub> NDs. The only difference in these procedures was the amount of BTBC. The mixed-phase SnSe–SnSe<sub>2</sub> NDs and the pure SnSe NSs were obtained by increasing the level of BTBC to 200 and 500 mg, respectively.

**Synthesis of SnSe<sub>2</sub> Control Sample.** In the control experiment, that without TOP and using only BTBC as the capping reagent, the Se powder was selected as the selenium source. The detailed synthetic and post-treatment procedures were similar to those for SnSe<sub>2</sub> NDs. The only difference was that no TOP was used in this case.

**Characterizations.** The X-ray energy dispersive spectra were taken on a JSM-5610LV-Vantage type energy spectrometer. X-ray diffraction patterns were recorded on a powder sample using a D/max 2500 VL/PC diffractometer (Japan) equipped with graphite-monochromatized Cu Kα radiation in 2θ ranging from 10° to 90°. Related work voltage and current were 40 kV and 100 mA, respectively. The XPS data were acquired on a scanning X-ray microprobe (PHI 5000 Versa, ULAC-PHI, Inc.) using Al Kα radiation. Binding energies of Sn 3d and Se 3d were calibrated using the C 1s peak (BE = 284.6 eV) as standard. FE-SEM images were taken on a field-emission scanning electron microscope (JSM-7600F, Japan), operating at an accelerating voltage of 10 kV. The atomic force microscope studies were performed by means of a Nanoscope IIIa scanning probe microscope (Agilent, USA) under tapping mode. The transmission



electron microscopy images were taken on a JEOL-2100F apparatus at an accelerating voltage of 200 kV. The Fourier transform infrared spectra were collected on a Nexus 670 spectrometer.

**Electrochemical Tests for the Three-Electrode SC System.** The electrochemical performances were first carried out in a three-electrode system with a KOH electrolyte solution (6 M). The as-prepared SnSe<sub>2</sub> NDs or mixed-phase SnSe–SnSe<sub>2</sub> NDs or SnSe NSs on nickel foam, a platinum wire, and a saturated calomel electrode (SCE) were used as the working electrode, counter electrode, and reference electrode, respectively. The working electrode was composed of active SnSe<sub>2</sub> NDs or SnSe NSs or mixed-phase SnSe–SnSe<sub>2</sub> ND material (70 wt %), conductive material (ATB, 20 wt %), and binder (PTFE, 10 wt %). The mixture was first coated onto the surface of a piece of nickel foam sheet (1 cm × 1 cm) and then dried at 50 °C under vacuum for 12 h. The cyclic voltammograms and galvanostatic charge–discharge tests were performed at 25 °C on a CHI 660D electrochemical workstation (Shanghai, Chenchua Co.).

**Fabrication and Electrochemical Tests for All-Solid-State Flexible SCs.** The PET substrates were first deposited with a layer of Pt film (~3–5 nm thick) and then coated with the slurry containing the active materials *via* a similar process to that in the three-electrode system and were used as the working electrode after drying. Subsequently, two pieces of such electrodes were immersed in the PVA/H<sub>2</sub>SO<sub>4</sub> gel solution for 5–10 min to adsorb a layer of solid electrolyte. After the excess water was vaporized, two pieces of such electrodes containing electrolyte were pressed together on a sheeting-out roller. Thus, the stacked all-solid-state SCs were fabricated, which were then evaluated for their supercapacitive performance on an Autolab (The Netherlands) electrochemical workstation in a two-electrode system. The CVs at different scan rates and bending angles were recorded at the potential from –0.40 to 0.40 V for SnSe<sub>2</sub> ND- and –0.55 to 0.55 V for SnSe NS-based solid-state devices, respectively. The galvanostatic charge–discharge curves were tested at various current densities. The PVA/H<sub>2</sub>SO<sub>4</sub> gel electrolyte was prepared as follows: 6 g of H<sub>2</sub>SO<sub>4</sub> was added into 60 mL of deionized water, and then 6 g of PVA powder was added. The whole mixture was heated to 85 °C under stirring until the solution became clear.

**Conflict of Interest:** The authors declare no competing financial interest.

**Acknowledgment.** This work was supported by the National Natural Science Foundation of China for project nos. 21271105, 21175069, 21171096, and 20901041, the research fund from the Priority Academic Program Development of Jiangsu Higher Education Institutions, and the opening research foundations of State Key Laboratory of Coordination Chemistry, Nanjing National Laboratory of Solid State Microstructures, Nanjing University.

**Supporting Information Available:** XPS spectra, AFM images, and FT-IR spectra of pure SnSe<sub>2</sub> NDs and SnSe NSs, control experimental results, microstructural and electrochemical data for mixed-phase SnSe–SnSe<sub>2</sub> NDs, structural characterization of pure SnSe<sub>2</sub> NDs and SnSe NSs after stability tests, and additional electrochemical data for SnSe<sub>2</sub> ND- and SnSe NS-based solid-state devices. This material is available free of charge *via* the Internet at <http://pubs.acs.org>.

## REFERENCES AND NOTES

1. Miller, J. R.; Simon, P. Electrochemical Capacitors for Energy Management. *Science* **2008**, *321*, 651–652.
2. Liu, C.; Li, F.; Ma, L. P.; Cheng, H. M. Advanced Materials for Energy Storage. *Adv. Mater.* **2010**, *22*, E28–E62.
3. Li, Q.; Wang, Z. L.; Li, G. R.; Guo, R.; Ding, L. X.; Tong, Y. X. Design and Synthesis of MnO<sub>2</sub>/Mn/MnO<sub>2</sub> Sandwich-Structured Nanotube Arrays with High Supercapacitive Performance for Electrochemical Energy Storage. *Nano Lett.* **2012**, *12*, 3803–3807.
4. Izadi-Najafabadi, A.; Yasuda, S.; Kobashi, K.; Yamada, T.; Futaba, D. N.; Hatori, H.; Yumura, M.; Iijima, S.; Hata, K.

- Extracting the Full Potential of Single-Walled Carbon Nanotubes as Durable Supercapacitor Electrodes Operable at 4 V with High Power and Energy Density. *Adv. Mater.* **2010**, *22*, E235–E241.
5. Boukhalifa, S.; Evanoff, K.; Yushin, G. Atomic Layer Deposition of Vanadium Oxide on Carbon Nanotubes for High-Power Supercapacitor Electrodes. *Energy Environ. Sci.* **2012**, *5*, 6872–6879.
6. Yan, J.; Fan, Z. J.; Sun, W.; Ning, G. Q.; Wei, T.; Zhang, Q.; Zhang, R. F.; Zhi, L. J.; Wei, F. Advanced Asymmetric Supercapacitors Based on Ni(OH)<sub>2</sub>/Graphene and Porous Graphene Electrodes with High Energy Density. *Adv. Funct. Mater.* **2012**, *22*, 2632–2641.
7. Lee, J. W.; Hall, A. S.; Kim, J. D.; Mallouk, T. E. A Facile and Template-Free Hydrothermal Synthesis of Mn<sub>3</sub>O<sub>4</sub> Nanorods on Graphene Sheets for Supercapacitor Electrodes with Long Cycle Stability. *Chem. Mater.* **2012**, *24*, 1158–1164.
8. Meng, C. Z.; Liu, C. H.; Chen, L. Z.; Hu, C. H.; Fan, S. S. Highly Flexible and All-Solid-State Paperlike Polymer Supercapacitors. *Nano Lett.* **2010**, *10*, 4025–4031.
9. Yoo, J. J.; Balakrishnan, K.; Huang, J. S.; Meunier, V.; Sumpter, B. G.; Srivastava, A.; Conway, M.; Reddy, A. L. M.; Yu, J.; Vajtai, R.; *et al.* Ultrathin Planar Graphene Supercapacitors. *Nano Lett.* **2011**, *11*, 1423–1427.
10. El-Kady, M. F.; Strong, V.; Dubin, S.; Kaner, R. B. Laser Scribing of High-Performance and Flexible Graphene-Based Electrochemical Capacitors. *Science* **2012**, *335*, 1326–1330.
11. Yuan, C. Z.; Yang, L.; Hou, L. R.; Li, J. Y.; Sun, Y. X.; Zhang, X. G.; Shen, L. F.; Lu, X. J.; Xiong, S. L.; Lou, X. W. Flexible Hybrid Paper Made of Monolayer Co<sub>3</sub>O<sub>4</sub> Microsphere Arrays on rGO/CNTs and Their Application in Electrochemical Capacitors. *Adv. Funct. Mater.* **2012**, *22*, 2560–2566.
12. Xiao, X.; Li, T. Q.; Yang, P. H.; Gao, Y.; Jin, H. Y.; Ni, W. J.; Zhan, W. H.; Zhang, X. H.; Cao, Y. Z.; Zhong, J. W.; *et al.* Fiber-Based All-Solid-State Flexible Supercapacitors for Self-Powered Systems. *ACS Nano* **2012**, *6*, 9200–9206.
13. Wang, K.; Meng, Q. H.; Zhang, Y. J.; Wei, Z. X.; Miao, M. H. High-Performance Two-Ply Yarn Supercapacitors Based on Carbon Nanotubes and Polyaniline Nanowire Arrays. *Adv. Mater.* **2013**, *25*, 1494–1498.
14. Wu, C. Z.; Lu, X. L.; Peng, L. L.; Xu, K.; Peng, X.; Huang, J. L.; Yu, H.; Xie, Y. Two-Dimensional Vanadyl Phosphate Ultrathin Nanosheets for High Energy Density and Flexible Pseudocapacitors. *Nat. Commun.* **2013**, *4*, 2431.
15. Wang, G. P.; Zhang, L.; Zhang, J. J. A Review of Electrode Materials for Electrochemical Supercapacitors. *Chem. Soc. Rev.* **2012**, *41*, 797–828.
16. Song, M. K.; Cheng, S.; Chen, H. Y.; Qin, W. T.; Nam, K. W.; Xu, S. C.; Yang, X. Q.; Bongiorno, A.; Lee, J.; Bai, J. M.; *et al.* Anomalous Pseudocapacitive Behavior of a Nanostructured, Mixed Valent Manganese Oxide Film for Electrical Energy Storage. *Nano Lett.* **2012**, *12*, 3483–3490.
17. Ren, J.; Bai, W. Y.; Guan, G. Z.; Zhang, Y.; Peng, H. S. Flexible and Weaveable Capacitor Wire Based on a Carbon Nanocomposite Fiber. *Adv. Mater.* **2013**, *25*, 5965–5970.
18. Zhu, Y. W.; Murali, S.; Stoller, M. D.; Ganesh, K. J.; Cai, W. W.; Ferreira, P. J.; Pirkle, A.; Wallace, R. M.; Cychosz, K. A.; Thommes, M.; *et al.* Carbon-Based Supercapacitor Produced by Activation of Graphene. *Science* **2011**, *332*, 1537–1541.
19. Huang, X.; Yin, Z. Y.; Wu, S. X.; Qi, X. Y.; He, Q. Y.; Zhang, Q. C.; Yan, Q. Y.; Boey, F.; Zhang, H. Graphene-Based Materials: Synthesis, Characterization, Properties, and Applications. *Small* **2011**, *7*, 1876–1902.
20. Cao, X. H.; Shi, Y. M.; Shi, W. H.; Lu, G.; Huang, X.; Yan, Q. Y.; Zhang, Q. C.; Zhang, H. Preparation of Novel 3D Graphene Networks for Supercapacitor Applications. *Small* **2011**, *7*, 3163–3168.
21. Wen, Z. H.; Wang, X. C.; Mao, S.; Bo, Z.; Kim, H.; Cui, S. M.; Lu, G. H.; Feng, X. L.; Chen, J. H. Crumpled Nitrogen-Doped Graphene Nanosheets with Ultrahigh Pore Volume for High-Performance Supercapacitor. *Adv. Mater.* **2012**, *24*, 5610–5616.

22. Huang, X.; Qi, X. Y.; Boey, F.; Zhang, H. Graphene-Based Composites. *Chem. Soc. Rev.* **2012**, *41*, 666–686.
23. Dong, X. C.; Xu, H.; Wang, X. W.; Huang, Y. X.; Chan-Park, M. B.; Zhang, H.; Wang, L. H.; Huang, W.; Chen, P. 3D Graphene-Cobalt Oxide Electrode for High-Performance Supercapacitor and Enzymeless Glucose Detection. *ACS Nano* **2012**, *6*, 3206–3213.
24. Zhou, W. J.; Cao, X. H.; Zeng, Z. Y.; Shi, W. H.; Zhu, Y. Y.; Yan, Q. Y.; Liu, H.; Wang, J. Y.; Zhang, H. One-Step Synthesis of  $\text{Ni}_3\text{S}_2$  Nanorod @  $\text{Ni}(\text{OH})_2$  Nanosheet Core-Shell Nanostructures on a Three-Dimensional Graphene Network for High-Performance Supercapacitors. *Energy Environ. Sci.* **2013**, *6*, 2216–2221.
25. Liu, X. H.; Ma, R. Z.; Bando, Y.; Sasaki, T. A General Strategy to Layered Transition-Metal Hydroxide Nanocones: Tuning the Composition for High Electrochemical Performance. *Adv. Mater.* **2012**, *24*, 2148–2153.
26. Xie, J. F.; Sun, X.; Zhang, N.; Xu, K.; Zhou, M.; Xie, Y. Layer-by-Layer  $\beta\text{-Ni}(\text{OH})_2$ /Graphene Nanohybrids for Ultraflexible All-Solid-State Thin-Film Supercapacitors with High Electrochemical Performance. *Nano Energy* **2013**, *2*, 65–74.
27. Guan, C.; Li, X. L.; Wang, Z. L.; Cao, X. H.; Soci, C.; Zhang, H.; Fan, H. J. Nanoporous Walls on Macroporous Foam: Rational Design of Electrodes to Push Areal Pseudocapacitance. *Adv. Mater.* **2012**, *24*, 4186–4190.
28. Yuan, C. Z.; Yang, L.; Hou, L. R.; Shen, L. F.; Zhang, X. G.; Lou, X. W. Growth of Ultrathin Mesoporous  $\text{Co}_3\text{O}_4$  Nanosheet Arrays on Ni Foam for High-Performance Electrochemical Capacitors. *Energy Environ. Sci.* **2012**, *5*, 7883–7887.
29. Peng, L. L.; Peng, X.; Liu, B. R.; Wu, C. Z.; Xie, Y.; Yu, G. H. Ultrathin Two-Dimensional  $\text{MnO}_2$ /Graphene Hybrid Nanostructures for High-Performance, Flexible Planar Supercapacitors. *Nano Lett.* **2013**, *13*, 2151–2157.
30. Yan, W. B.; Kim, J. Y.; Xing, W. D.; Donavan, K. C.; Ayvazian, T.; Penner, R. M. Lithographically Patterned Gold/Manganese Dioxide Core/Shell Nanowires for High Capacity, High Rate, and High Cyclability Hybrid Electrical Energy Storage. *Chem. Mater.* **2012**, *24*, 2382–2390.
31. Wang, Q. H.; Kalantar-Zadeh, K.; Kis, A.; Coleman, J. N.; Strano, M. S. Electronics and Optoelectronics of Two-Dimensional Transition Metal Dichalcogenides. *Nat. Nanotechnol.* **2012**, *7*, 699–712.
32. Chhowalla, M.; Shin, H. S.; Eda, G.; Li, L. J.; Loh, K. P.; Zhang, H. The Chemistry of Two-Dimensional Layered Transition Metal Dichalcogenide Nanosheets. *Nat. Chem.* **2013**, *5*, 263–275.
33. Zhang, X. D.; Xie, Y. Recent Advances in Free-Standing Two-Dimensional Crystals with Atomic Thickness: Design, Assembly and Transfer Strategies. *Chem. Soc. Rev.* **2013**, *42*, 8187–8199.
34. Huang, X.; Zeng, Z. Y.; Zhang, H. Metal Dichalcogenide Nanosheets: Preparation, Properties and Applications. *Chem. Soc. Rev.* **2013**, *42*, 1934–1946.
35. Sun, Y. F.; Gao, S.; Xie, Y. Atomically-Thick Two-Dimensional Crystals: Electronic Structure Regulation and Energy Device Construction. *Chem. Soc. Rev.* **2014**, *43*, 530–546.
36. Feng, J.; Sun, X.; Wu, C. Z.; Peng, L. L.; Lin, C. W.; Hu, S. L.; Yang, J. L.; Xie, Y. Metallic Few-Layered  $\text{VS}_2$  Ultrathin Nanosheets: High Two-Dimensional Conductivity for In-Plane Supercapacitors. *J. Am. Chem. Soc.* **2011**, *133*, 17832–17838.
37. Rao, T. S.; Chaudhuri, A. K. Photoconductive Relaxation Studies of SnSe Thin Films. *Bull. Mater. Sci.* **1996**, *19*, 449–453.
38. Yu, X. C.; Zhu, J.; Zhang, Y. H.; Weng, J.; Hu, L. H.; Dai, S. Y. SnSe<sub>2</sub> Quantum Dot Sensitized Solar Cells Prepared Employing Molecular Metal Chalcogenide as Precursors. *Chem. Commun.* **2012**, *48*, 3324–3326.
39. Franzman, M. A.; Schlenker, C. W.; Thompson, M. E.; Brutchey, R. L. Solution-Phase Synthesis of SnSe Nanocrystals for Use in Solar Cells. *J. Am. Chem. Soc.* **2010**, *132*, 4060–4061.
40. Wang, R. Y.; Caldwell, M. A.; Jeyasingh, R. G. D.; Aloni, S.; Shelby, R. M.; Wong, H. S. P.; Milliron, D. J. Electronic and Optical Switching of Solution-Phase Deposited SnSe<sub>2</sub> Phase Change Memory Material. *J. Appl. Phys.* **2011**, *109*, 113506–113512.
41. Choi, J.; Jin, J.; Jung, I. G.; Kim, J. M.; Kim, H. J.; Son, S. U. SnSe<sub>2</sub> Nanoplate-Graphene Composites as Anode Materials for Lithium Ion Batteries. *Chem. Commun.* **2011**, *47*, 5241–5243.
42. Jang, K.; Lee, I. Y.; Xu, J.; Choi, J.; Jin, J.; Park, J. H.; Kim, H. J.; Kim, G. H.; Son, S. U. Colloidal Synthesis of SnSe Nanocolumns through Tin Precursor Chemistry and Their Optoelectrical Properties. *Cryst. Growth Des.* **2012**, *12*, 3388–3391.
43. Baumgardner, W. J.; Choi, J. J.; Lim, Y. F.; Hanrath, T. SnSe Nanocrystals: Synthesis, Structure, Optical Properties, and Surface Chemistry. *J. Am. Chem. Soc.* **2010**, *132*, 9519–9521.
44. Liu, S.; Guo, X. Y.; Li, M. R.; Zhang, W. H.; Liu, X. Y.; Li, C. Solution-Phase Synthesis and Characterization of Single-Crystalline SnSe Nanowires. *Angew. Chem., Int. Ed.* **2011**, *50*, 12050–12053.
45. Huang, L.; Yu, Y. F.; Li, C.; Cao, L. Y. Substrate Mediation in Vapor Deposition Growth of Layered Chalcogenide Nanoplates: A Case Study of SnSe<sub>2</sub>. *J. Phys. Chem. C* **2013**, *117*, 6469–6475.
46. Vaughn, D. D.; In, S. I.; Schaak, R. E. A Precursor-Limited Nanoparticle Coalescence Pathway for Tuning the Thickness of Laterally-Uniform Colloidal Nanosheets: The Case of SnSe. *ACS Nano* **2011**, *5*, 8852–8860.
47. Li, L.; Chen, Z.; Hu, Y.; Wang, X. W.; Zhang, T.; Chen, W.; Wang, Q. B. Single-Layer Single-Crystalline SnSe Nanosheets. *J. Am. Chem. Soc.* **2013**, *135*, 1213–1216.
48. Cavallo, F.; Lagally, M. G. Semiconductors Turn Soft: Inorganic Nanomembranes. *Soft Matter* **2010**, *6*, 439–455.
49. Radisavljevic, B.; Radenovic, A.; Brivio, J.; Giacometti, V.; Kis, A. Single-Layer  $\text{MoS}_2$  Transistors. *Nat. Nanotechnol.* **2011**, *6*, 147–150.
50. Wang, X. F.; Liu, B.; Wang, Q. F.; Song, W. F.; Hou, X. J.; Chen, D.; Cheng, Y. B.; Shen, G. Z. Three-Dimensional Hierarchical GeSe<sub>2</sub> Nanostructures for High Performance Flexible All-Solid-State Supercapacitors. *Adv. Mater.* **2013**, *25*, 1479–1486.
51. Sines, I. T.; Schaak, R. E. Phase-Selective Chemical Extraction of Selenium and Sulfur from Nanoscale Metal Chalcogenides: A General Strategy for Synthesis, Purification and Phase Targeting. *J. Am. Chem. Soc.* **2011**, *133*, 1294–1297.
52. Dong, S. M.; Chen, X. A.; Gu, L.; Zhou, X. H.; Xu, H. X.; Wang, H. B.; Liu, Z. H.; Han, P. X.; Yao, J. H.; Wang, L.; et al. Facile Preparation of Mesoporous Titanium Nitride Microspheres for Electrochemical Energy Storage. *ACS Appl. Mater. Interface* **2011**, *3*, 93–98.
53. Wang, B.; Park, J.; Su, D. W.; Wang, C. Y.; Ahn, H.; Wang, G. X. Solvothermal Synthesis of  $\text{CoS}_2$ -Graphene Nanocomposite Material for High-Performance Supercapacitors. *J. Mater. Chem.* **2012**, *22*, 15750–15756.
54. Fan, Z. J.; Yan, J.; Wei, T.; Zhi, L. J.; Ning, G. Q.; Li, T. Y.; Wei, F. Asymmetric Supercapacitors Based on Graphene/ $\text{MnO}_2$  and Activated Carbon Nanofiber Electrodes with High Power and Energy Density. *Adv. Funct. Mater.* **2011**, *21*, 2366–2375.
55. Yang, Z. S.; Chen, C. Y.; Chang, H. T. Supercapacitors Incorporating Hollow Cobalt Sulfide Hexagonal Nanosheets. *J. Power Sources* **2011**, *196*, 7874–7877.
56. Lang, X. Y.; Hirata, A.; Fujita, T.; Chen, M. W. Nanoporous Metal/Oxide Hybrid Electrodes for Electrochemical Supercapacitors. *Nat. Nanotechnol.* **2011**, *6*, 232–236.
57. Yang, L.; Cheng, S.; Ding, Y.; Zhu, X. B.; Wang, Z. L.; Liu, M. L. Hierarchical Network Architectures of Carbon Fiber Paper Supported Cobalt Oxide Nanonet for High-Capacity Pseudocapacitors. *Nano Lett.* **2012**, *12*, 321–325.
58. Subramanian, V.; Zhu, H. W.; Vajtai, R.; Ajayan, P. M.; Wei, B. Q. Hydrothermal Synthesis and Pseudocapacitance Properties of  $\text{MnO}_2$  Nanostructures. *J. Phys. Chem. B* **2005**, *109*, 20207–20214.